

VARIABILITY PROFILES OF MILLISECOND X-RAY PULSARS: RESULTS OF PSEUDO-NEWTONIAN THREE-DIMENSIONAL MAGNETOHYDRODYNAMIC SIMULATIONS

A. K. KULKARNI AND M. M. ROMANOVA

Department of Astronomy, Cornell University, 611 Space Sciences Building, Ithaca, NY 14853; akshay@astro.cornell.edu,
romanova@astro.cornell.edu

Received 2004 December 21; accepted 2005 June 17

ABSTRACT

We model the variability profiles of millisecond-period X-ray pulsars. We performed three-dimensional magnetohydrodynamic simulations of disk accretion to millisecond-period neutron stars with a misaligned magnetic dipole moment, using the pseudo-Newtonian Paczyński-Wiita potential to model general relativistic effects. We found that the shapes of the resulting funnel streams of accreting matter and the hot spots on the surface of the star are quite similar to those for more slowly rotating stars obtained from earlier simulations using the Newtonian potential. The funnel streams and hot spots rotate approximately with the same angular velocity as the star. The spots are bow-shaped (bar-shaped) for small (large) misalignment angles. We found that the matter falling on the star has a higher Mach number when we use the Paczyński-Wiita potential than in the Newtonian case. Having obtained the surface distribution of the emitted flux, we calculated the variability curves of the star, taking into account general relativistic, Doppler, and light-travel time effects. We found that general relativistic effects decrease the pulse fraction (flatten the light curve), while Doppler and light-travel time effects increase it and distort the light curve. We also found that the light curves from our hot spots are reproduced reasonably well by spots with a Gaussian flux distribution centered at the magnetic poles. We also calculated the observed image of the star in a few cases and saw that for certain orientations, both the antipodal hot spots are simultaneously visible, as noted by earlier authors.

Subject headings: accretion, accretion disks — pulsars: general — X-rays: stars

1. INTRODUCTION

Millisecond X-ray pulsars show bursts of periodic and quasi-periodic variability in the X-ray (Stella & Vietri 1999; van der Klis 2000; Chakrabarty et al. 2003; Wijnands et al. 2003). Six of these pulsars are believed to be accretion powered (Wijnands 2005). Numerical modeling of accretion is an important tool for studying these phenomena. Three-dimensional magnetohydrodynamic (MHD) simulations of disk accretion to rotating magnetized stars with a misaligned dipole magnetic field have been carried out by Koldoba et al. (2002) and Romanova et al. (2003; 2004, hereafter R04). They found that the accreting matter is channeled by the star’s magnetic field into two antipodal streams or funnels and falls on the stellar surface forming two antipodal hot spots—regions of relatively high temperature. Such flows have been predicted theoretically (e.g., Pringle & Rees 1972; Lamb et al. 1973; Ghosh & Lamb 1978, 1979) but were modeled numerically only recently. Assuming that the energy of the infalling matter is converted entirely into radiation, R04 then calculated the variability curves of the star. Those simulations and calculations were performed for a generic star in a completely classical framework. We refined those simulations, focusing on rapidly rotating (~ 3 – 5 ms period) neutron stars. For such stars, the following issues arise: (1) For compact objects such as neutron stars, general relativistic effects significantly influence the accretion process, as well as the observed flux. (i) We modeled general relativistic effects on accretion by using the pseudo-Newtonian Paczyński-Wiita potential (Paczyński & Wiita 1980), which reproduces some important features of the Schwarzschild geometry, such as the positions of the innermost stable and marginally bound circular orbits. (ii) The variability curve of the star also changes significantly because gravitational bending of light emitted by the star allows more of the star than the hemisphere facing the observer to be visible, and gravitational red-

shift of the light decreases the total flux observed. We use the Schwarzschild metric to take these effects into account. (2) For rapidly rotating stars such as millisecond pulsars, the rotation of the star changes the observed flux through the twin special relativistic effects of Doppler shift and relativistic beaming of the emitted radiation. Henceforth, we refer to these two effects collectively as the “Doppler effect.” (3) The time difference between light emitted from different points on the star reaching the observer is important when the linear speed of the emitting region is comparable to the speed of light, and also when the emitting object is compact, and it causes distortion of the observed shape of the hot spots (the apparent position of a point on the stellar surface can differ by as much as 10° from its actual position). We build upon the earlier calculations to take these effects into account. In addition, due to the high rotation speed, the Kerr metric would be closer to the actual metric around the star than the Schwarzschild metric. However, we do not use the Kerr metric, since we find from numerical integrations that the frame-dragging effects introduced by the Kerr metric are relatively small (see also Braje et al. 2000), particularly when compared with the other errors introduced by the assumptions in our variability model.

These effects on the light curves have been taken into account by earlier authors to obtain light curves for simple hot spots (see, e.g., Pechenick et al. 1983; Ftaclas et al. 1986; Braje et al. 2000; Ford 2000; Beloborodov 2002; Poutanen & Gierlinski 2003; Viironen & Poutanen 2004; Bhattacharyya et al. 2005). Here we obtain light curves using realistic hot spots obtained from our accretion simulations.

In § 2 we present the results of our MHD simulations. We then discuss the analytical background for calculating variability curves in § 3 and show the variability curves for synthetic and realistic spots in §§ 4 and 5, respectively, followed by some concluding remarks in § 6.

2. DISK ACCRETION—THREE-DIMENSIONAL SIMULATIONS

2.1. Earlier Simulations

We briefly describe earlier three-dimensional MHD simulations (Koldoba et al. 2002; Romanova et al. 2003; R04). The star has a dipole magnetic field, the axis of which makes an angle Θ with the star's rotation axis. The rotation axes of the star and the accretion disk are aligned. The disk has a low-density corona that also rotates about the same axis. To model stationary accretion, the disk was chosen to initially be in a quasi-equilibrium state, where the gravitational, centrifugal, and pressure gradient forces are in balance (Romanova et al. 2002). Viscosity is modeled using the α -model (Novikov & Thorne 1973; Shakura & Sunyaev 1973). To model accretion, the ideal MHD equations were solved numerically in three dimensions, using a Godunov-type numerical code, written in a “cubed-sphere” coordinate system rotating with the star (Koldoba et al. 2002; Romanova et al. 2003). The boundary conditions at the star's surface amount to assuming that the infalling matter passes through the surface of the star. Thus, the dynamics of the matter after it falls on the star was ignored. It was found that the inward motion of the accretion disk is stopped by the star's magnetosphere at the Alfvén radius, where the magnetic and matter energy densities become equal. At that point the matter leaves the disk and moves along the magnetic field lines. This flow is called a funnel stream. In this region, the matter radiates primarily in the X-ray. It heats up the star's surface where it falls, forming “hot spots.” There are two antipodal funnel streams and hot spots. From the point of view of an external observer, they rotate with approximately the same angular velocity as the star, causing the observed flux to vary periodically with time. The shape of the funnel streams and hot spots keeps changing slightly with time, leading to quasi variability in the observed flux.

2.2. Reference Values

In our new simulations, we use the same model as described above. The simulations use the following dimensionless variables: the radial coordinate $r' = r/R_0$, the fluid velocity $\mathbf{v}' = \mathbf{v}/v_0$, the density $\rho' = \rho/\rho_0$, the magnetic field $\mathbf{B}' = \mathbf{B}/B_0$, the pressure $p' = p/p_0$, the temperature $T' = T/T_0$, and the time $t' = t/t_0$. The variables with subscript 0 are dimensional reference values, and the unprimed variables are the dimensional variables. Because of the use of dimensionless variables, the results are applicable to a wide range of objects and physical conditions, each with its own set of reference values. To apply our simulation results to a particular situation, we have the freedom to choose three parameters, and all the reference values are calculated from those. We choose the mass, radius, and surface magnetic field of the star as the three independent parameters.

The reference values are determined as follows: The unit of distance R_0 is chosen such that the star has radius $R = 0.35R_0$. The reference velocity is the Keplerian velocity at R_0 , $v_0 = (GM/R_0)^{1/2}$, and $\omega_0 = v_0/R_0$ is the reference angular velocity. The reference time is $t_0 = R_0/v_0$. The reference surface magnetic field of the star is B_{*0} . The reference magnetic field, B_0 , is the initial magnetic field strength at $r = R_0$, assuming a surface magnetic field of B_{*0} . The reference density is taken to be $\rho_0 = B_0^2/v_0^2$. The reference pressure is $p_0 = \rho_0 v_0^2$. The reference temperature is $T_0 = p_0/\mathcal{R}\rho_0$, where \mathcal{R} is the gas constant. The reference accretion rate is $\dot{M}_0 = \rho_0 v_0 R_0^2$. The reference energy flux is $\dot{E}_0 = \rho_0 v_0^3 R_0^2$. The reference value for the effective blackbody temperature of the hot spots is $(T_{\text{eff}})_0 = (\rho_0 v_0^3/\sigma)^{1/4}$, where σ is the Stefan-Boltzmann constant.

For the millisecond pulsars in our simulations, we take the mass of the neutron star to be $M = 1.4 M_\odot = 2.8 \times 10^{33}$ g, and its radius $R = 10$ km = 10^6 cm. The reference length scale is $R_0 \approx 2.86R = 2.86 \times 10^6$ cm. The reference velocity is $v_0 = 8.1 \times 10^9$ cm s⁻¹. The reference time is $t_0 = 0.35$ ms. The reference surface magnetic field is $B_{*0} = 10^8$ G, which is a typical value for millisecond pulsars. Then the reference magnetic field is $B_0 = B_{*0}(R/R_0)^3 \approx 4.3 \times 10^6$ G. The reference density is $\rho_0 = 2.8 \times 10^{-7}$ g cm⁻³. The reference pressure is $p_0 = 1.8 \times 10^{13}$ dynes cm⁻². The reference temperature is $T_0 = 7.9 \times 10^{11}$ K. The reference value of the effective blackbody temperature is $(T_{\text{eff}})_0 \approx 7.2 \times 10^6$ K. The reference mass accretion rate is $\dot{M}_0 \approx 1.85 \times 10^{16}$ g s⁻¹ $\approx 2.9 \times 10^{-10} M_\odot$ yr⁻¹. The reference energy flux is $\dot{E}_0 \approx 1.2 \times 10^{36}$ ergs s⁻¹. Subsequently, we drop the primes on the dimensionless variables and show dimensionless values in the figures.

2.3. New Simulations

We performed new simulations for rapidly rotating (3–5 ms period) neutron stars. We followed the same procedure as described above, with two major changes: (1) We modeled general relativistic effects on accretion by using the pseudo-Newtonian Paczyński-Wiita (PW) potential (Paczyński & Wiita 1980), $\Phi(r) = -GM/(r - r_g)$, where M is the mass of the star and $r_g = 2GM/c^2$ is its Schwarzschild radius. (2) We calculated the variability curves taking into account relativistic and light-travel time effects.

We used the following parameters in our simulations: The surface magnetic field of the star was 5×10^7 G. The star's Schwarzschild radius was $r_g = 4.15$ km = 4.15×10^5 cm, or 0.145 in dimensionless units. The disk and corona initially had temperatures of 0.01 and 1, respectively, and densities of 1 and 0.01, respectively. The disk was thinner than in the earlier simulations. The viscosity α -parameter was 0.04. Each of the six blocks of our cubed-sphere grid had 65 cells in the radial direction and 31 in the angular direction, which corresponds to an outer disk radius of ~ 8.7 , or about 25 stellar radii.

We used a modified code and modified initial conditions that use the PW potential instead of the Newtonian one. The initial values of physical variables in the disk do not change significantly due to use of the PW potential. We found that the shapes of the funnel streams and hot spots are similar to those in earlier simulations for more slowly rotating stars, and in simulations with the Newtonian potential. We also found that the velocity of the infalling matter near the surface of the star is higher in the “PW” case than in the “non-PW” case. This is expected because the PW potential is stronger than the Newtonian one.

The accretion rate is higher in the PW case than in the non-PW case, as Figure 1 shows. This is again expected because the PW potential is stronger. This will lead to faster depletion of the inner disk matter. If angular momentum is efficiently transported outward, e.g., by the magnetorotational instability (see, e.g., Hawley & Krolik 2001), then the influence of the PW potential will eventually be felt in the outer disk regions, and enhanced accretion could be sustained for a longer time.

The top row of Figure 2 shows the flow of matter around a star with $P = 3$ ms in the PW case. The flow is similar in the non-PW case. The next two rows show the hot spots formed on the surface of the star, without and with the PW potential. We see that the position and shape of the hot spots depend on the misalignment angle but do not significantly depend on the presence of the PW potential. The hot spots are bow shaped (bar shaped) for small (large) misalignment angles. The emitted flux is highest at the center of the spots and decreases outward. Note that the hot spots

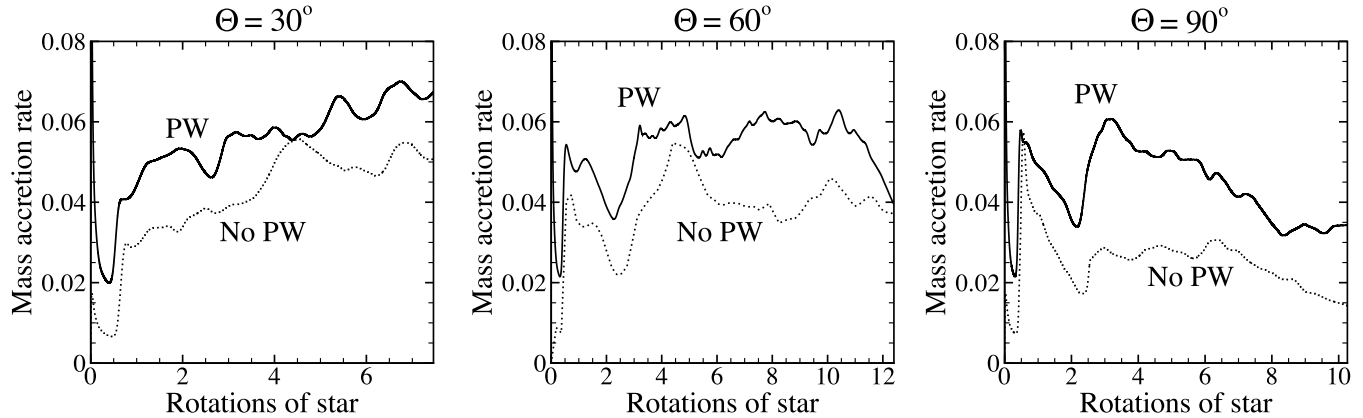


Fig. 1.—Mass accretion rates for a 3 ms pulsar with (solid lines) and without (dotted lines) the Paczyński-Wiita potential, for different misalignment angles.

are not usually centered at the magnetic poles. In fact, they do not even fall on the magnetic poles in most cases. We see that the emitted flux is higher in the PW case, which is expected because the PW potential is stronger than the Newtonian one.

To get an idea of the conditions at the surface of a larger neutron star with the same mass, rotation period, and magnetic dipole moment, in a similar situation, we can look at the surface of a sphere of radius 15 km concentric with the star in our simulations. This approach is valid because changing the star’s radius does not change the accretion flow around the star, since the PW potential depends only on the star’s Schwarzschild radius. The bottom row of Figure 2 shows the hot spots on such a sphere. We see that, other conditions remaining the same, a larger star has much fainter hot spots, which is again to be expected because the accreting matter has a lower velocity at the surface of the larger star.

For 3 ms pulsars, the typical values of physical quantities observed in our simulations after 4–6 rotations of the star are as follows: The surface magnetic field does not change in our model and hence is $\sim 5 \times 10^7$ G. The mass accretion rate to the star $\sim 10^{15}$ g s $^{-1}$ $\sim 10^{-12}$ M_{\odot} yr $^{-1}$. The total power emitted from the star, after correcting for gravitational redshift, $\sim 10^{34}$ ergs s $^{-1}$. In the hot spots, the matter density $\sim 10^{-7}$ g cm $^{-3}$. The speed of the inflowing matter $\sim 2 \times 10^{10}$ cm s $^{-1}$. The effective blackbody temperature of the hot spots $\sim 5 \times 10^6$ K. The matter pressure $\sim 10^{12}$ dynes cm $^{-2}$. The Mach number ~ 1 –6 in the PW case and ~ 0.8 –3 in the non-PW case. The surface distributions of the density, pressure, velocity, and temperature closely follow that of the emitted flux.

3. CALCULATION OF THE VARIABILITY CURVES

Having obtained the distribution of emitted flux on the star’s surface, we can calculate the flux received by an observer. Without including the relativistic and light-travel time effects, the observed flux at a large distance D from the star is proportional to

$$J = \int_{\cos \psi > 0} dS I_E(\mathbf{R}, \psi) \cos \psi, \quad (1)$$

where dS is an element of area of the star’s surface at a position \mathbf{R} and $I_E(\mathbf{R}, \psi)$ is the intensity of radiation emitted by dS at an angle ψ with respect to the local radial direction (Fig. 3a). We have ignored the overall factor of $1/D^2$ in the flux. When calculating this numerically, the integral becomes a sum over grid elements. We now consider the gravitational and rotational effects one by one. These calculations have been done by earlier authors (see, e.g., Poutanen & Gierlinski 2003; Viironen & Poutanen

2004), but we present them here for the sake of completeness and for discussing slight differences in approach.

3.1. General Relativistic Effects

When taking general relativistic effects into account, two approaches are possible toward calculating the observed flux. In the traditional ray-tracing method (see, e.g., Braje et al. 2000; Bhattacharyya et al. 2005), one traces light rays backward from the observer’s image plane to the star’s surface by numerically integrating the geodesic equations. The flux emitted from the point where a light ray meets the star will then determine the intensity of that ray. This can be called an “observer-centered” approach. For our purposes, however, it is more convenient to take a “grid-centered” approach, since our MHD simulations give us the hot spot data on a grid, and it is more convenient to calculate the contribution of each grid element to the observed flux and then sum over all grid elements, as stated above. So we use the following approach (see, e.g., Beloborodov 2002).

Because of light bending, the light from point B in Figure 3b needs to be emitted at an angle α such that after bending, it travels toward the observer; that is, it travels at an angle ψ with respect to the original radial direction. To calculate the observed flux, we need a relation between ψ and α . We use the Schwarzschild metric. From the geodesic equations, we then have (see, e.g., Misner et al. 1973; Pechenick et al. 1983)

$$\psi = \int_R^{\infty} \frac{dr}{r^2} \left[\frac{1}{b^2} - \frac{1}{r^2} \left(1 - \frac{r_g}{r} \right) \right]^{-1/2}, \quad (2)$$

where r is the radial Schwarzschild coordinate, R and r_g are the star’s radius and Schwarzschild radius, respectively, and b is the impact parameter. Using the four-velocity of a photon at the point of emission, we can relate b to α to get (see, e.g., Beloborodov 2002) $b = R(1 - r_g/R)^{-1/2} \sin \alpha$. We now have the desired relation between ψ and α . The integration in equation (2) cannot be done analytically but is relatively easy to do numerically. However, the problem in our case is a more difficult one because in the grid-centered approach we know ψ for each grid element, and we have to solve equation (2) for α . Computationally, this is very difficult to do exactly. So we use the cosine relation, an approximate relation (due to Beloborodov 2002), which has the advantages of being very simple to use and highly accurate:

$$1 - \cos \alpha \approx (1 - \cos \psi) \left(1 - \frac{r_g}{R} \right). \quad (3)$$

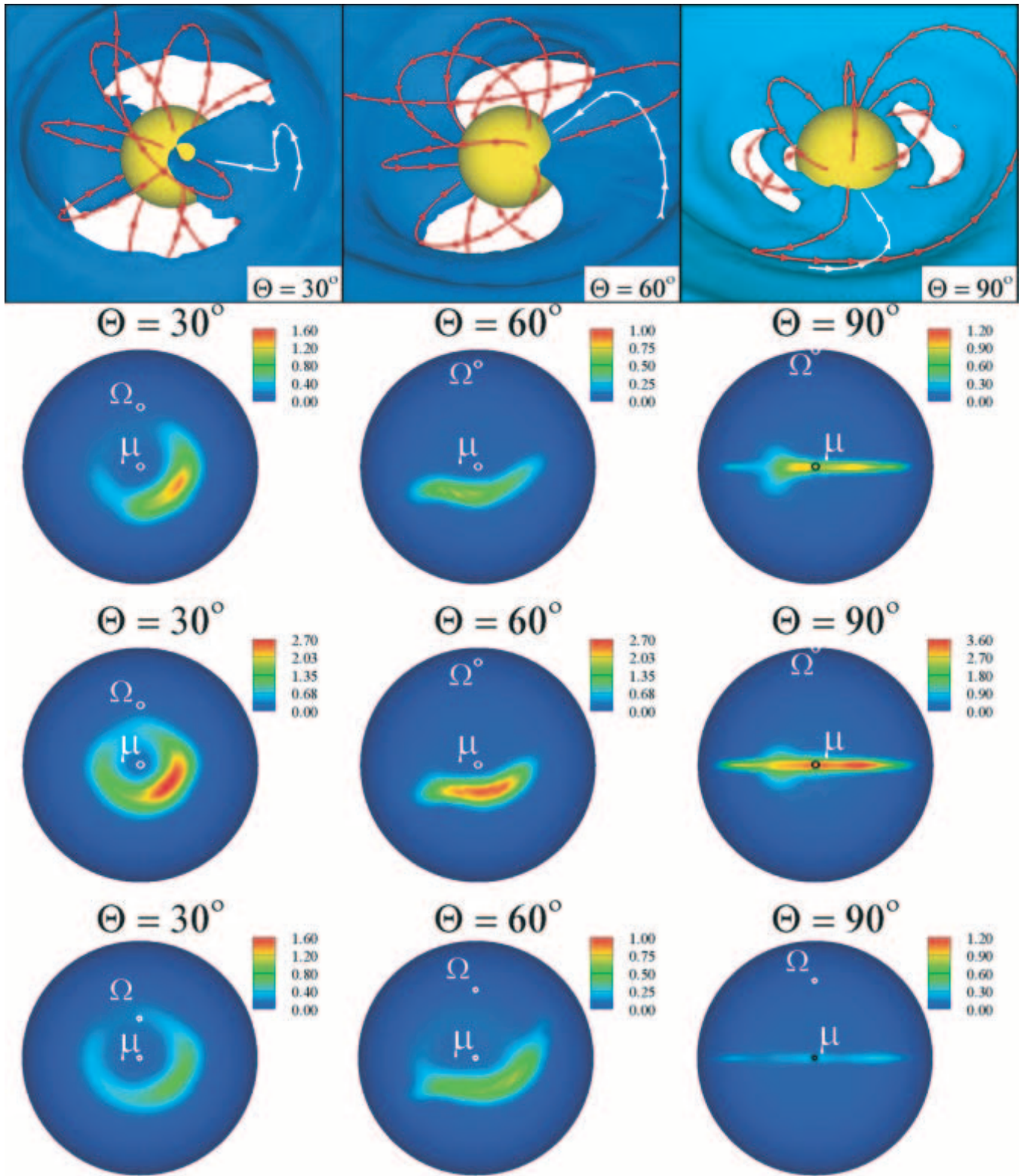


FIG. 2.—*Top row:* Matter flow around a star with $P = 3$ ms in the PW case for different misalignment angles. The red lines are sample magnetic field lines, and the white lines are sample streamlines of matter flow. *Second row:* Distribution of emitted flux on the star's surface, without using the PW potential. *Third row:* Distribution of emitted flux on the star's surface, using the PW potential. *Bottom row:* Distribution of emitted flux on a sphere of radius 15 km, using the PW potential.

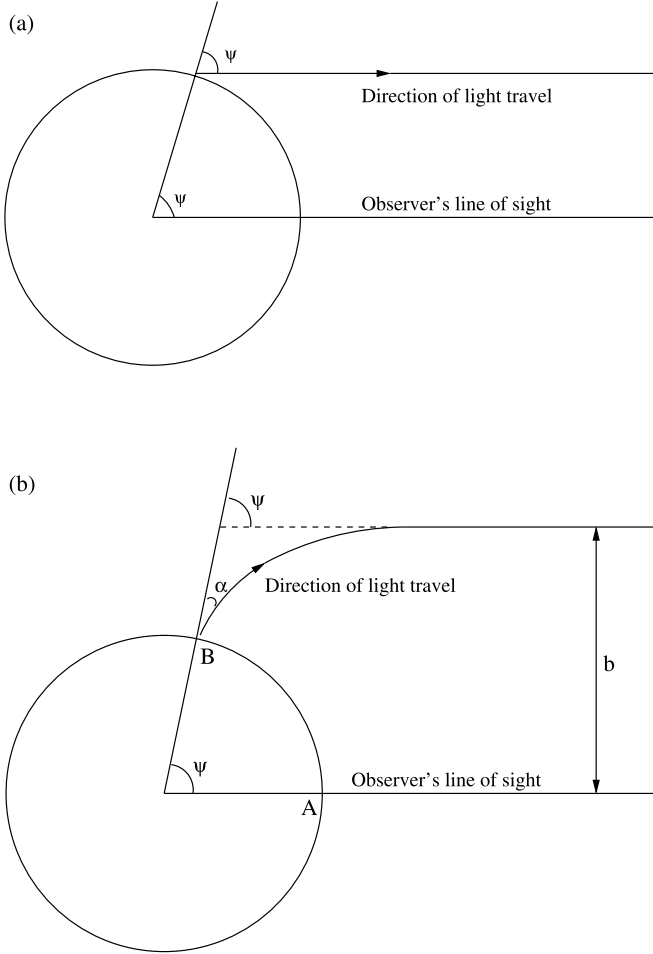


FIG. 3.—Path of light emitted by a compact object: (a) neglecting light bending, and (b) including light bending.

In that case the observed flux is given by (Beloborodov 2002)

$$J = \left(1 - \frac{r_g}{R}\right)^2 \int_{\cos \alpha > 0} dS I_E(\mathbf{R}, \alpha) \cos \alpha. \quad (4)$$

Thus, the angle ψ in equation (1) is replaced by α , and we get a prefactor of $(1 - r_g/R)^2$ due to gravitational redshift.

An interesting consequence of light bending is that the observer can see some radiation from the far side of the star (see, e.g., Beloborodov 2002). In particular, both the antipodal hot spots of pulsars can be seen simultaneously in some cases.

3.2. Doppler Effect

The above discussion is valid if $I_E(\mathbf{R}, \alpha)$ is the intensity in a reference frame that is at rest with respect to the observer. However, our MHD simulations calculate the intensity in a reference frame that is rotating with the star. We need to relate the intensities in these two frames. We use the invariance of I_ν/ν^3 along a ray of light, where I_ν is the specific intensity, or the intensity per unit frequency range. Then for a ray emitted from a point on the star that is moving with a velocity $v = \beta c$ and Lorentz factor $\gamma = (1 - \beta^2)^{-1/2}$, we have¹ $I_\nu = I'_\nu/\gamma^3(1 - \beta\mu)^3$, since ν and ν' are related by the Doppler formula $\nu' = \nu\gamma(1 - \beta\mu)$. Here $\mu = \cos \theta$,

where θ is the angle, as measured in the unprimed frame, between the direction of emission of the light and the direction of motion of the emitting surface element of the star. The direction of emission of light is given by equation (3). Integrating over frequency, we then have $I = I'/\gamma^4(1 - \beta\mu)^4$. Thus, in equation (4) for the observed flux, we pick up an extra factor of $1/\gamma^4(1 - \beta\mu)^4$. In addition, the areas of the hot spots as measured by photon beams in the two frames are related by $dS' = \gamma(1 - \beta\mu)dS$ (Terrell 1959). This is a consequence of the projected area $dS \cos \alpha$ being a Lorentz invariant. So the flux is now given by

$$J = \left(1 - \frac{r_g}{R}\right)^2 \int_{\cos \alpha > 0} dS' \frac{1}{\gamma^5(1 - \beta\mu)^5} I'_E(\mathbf{R}', \alpha') \cos \alpha. \quad (5)$$

3.3. Light-Travel Time Effects

Now we take into account the fact that light from different parts of the star takes different amounts of time to reach the observer. We need to use the general relativistic expression for the light-travel time, since we are dealing with a compact object. We again use the Schwarzschild metric. Using the geodesic equations, the time difference between light emitted from points A and B in Figure 3b reaching the observer is (assuming $D \gg R$)

$$\delta t(b) = \frac{1}{c} \int_R^\infty \frac{dr}{(1 - r_g/r)} \left\{ \left[1 - \frac{b^2}{r^2} \left(1 - \frac{r_g}{r}\right) \right]^{-1/2} - 1 \right\}. \quad (6)$$

We then need to find the apparent position of each grid element at a given time. At the time when point A in Figure 3b will appear to be at the center of the observer's image, point B will appear to be not where it is shown in the figure but where it was a time Δt ago, where Δt must satisfy

$$\delta t(b_{\Delta t}) = \Delta t. \quad (7)$$

Here $b_{\Delta t}$ is the impact parameter for light emitted from point B a time Δt ago. This determines the apparent position of grid element B at the time when grid element A is at the position shown in Figure 3b.

In the observer-centered approach, one needs to solve equation (6), which is relatively easy to do numerically. However, in the grid-centered approach, one has to solve equation (7), which, after substituting for $\delta t(b_{\Delta t})$ from equation (6), becomes an integral equation that cannot be solved analytically and is very difficult to solve numerically. Thus, following Beloborodov (2002), we expand the integrand in equation (6) in powers of $x = 1 - \cos \psi = (1 - \cos \alpha)/(1 - r_g/R)$ and then perform the integration. We keep as many terms as are needed for sufficient accuracy (accuracy can be checked by comparing the values obtained from the series with those obtained by integrating eq. [6] numerically). The resulting equation, although still implicit in Δt , is much easier to solve numerically. We can now calculate the apparent position of any grid point at any time and then compute the flux as given by equation (5) by summing over all grid elements.

3.4. Frame-Dragging Effects

The neutron stars considered in our simulations have $R = 10$ km and $M = 1.4 M_\odot$. The fastest rotators that we considered have $P = 3$ ms. For these parameters, we tried to find out the significance of frame dragging by numerically evaluating frame-dragging corrections to the path of light in the equatorial plane of the star, using the Kerr metric. We found that corrections to the angle α (Fig. 3b) are at most $\sim 4^\circ$. Corrections to the time delay δt

¹ Notation in this subsection: Unprimed quantities are those measured in a frame at rest (with respect to the observer) at the star's surface. Primed quantities are those measured in a frame rotating with the star.

(eq. [6]) are of the order of a few percent, which is not large considering the fact that the effect of time delay on the variability curve is itself quite small, as we see in § 5. The gravitational redshift factor has corrections of $\leq 1\%$. We thus expect the errors introduced by ignoring frame dragging to be much smaller than those introduced by the assumptions in our variability model (which we discuss in § 5). This, together with the fact that frame-dragging effects are very difficult to take into account numerically, is why we do not do so. Variability curves have been calculated by earlier authors taking these effects into account (Braje et al. 2000), and they found that the curves do not change significantly due to these effects.

4. EXAMPLES WITH SIMPLE SYNTHETIC SPOTS

4.1. Point Spot

It is clear from the foregoing discussion that general relativistic effects become stronger with increasing r_g , and Doppler and time-delay effects become stronger with increasing rotation speed of the star. To see clearly the effect of all these effects on the light curve, it is useful to consider the simple case of a point spot shown in Figure 4. We have only one spot, which is on the rotational equator of the star, and the observer is in the equatorial plane of the star. When no effects are included, the light curve is simply a half-sinusoid (due to the $\cos \psi$ factor in eq. [1]) with a maximum when the spot is at point C and minima when the spot is on the far side of the star (Fig. 5). The points labeling the curve correspond to the spot being at the respective points in Figure 4. Let us now look at all the effects separately.

Time delay.—Referring to Figure 4, the light from, say, point B takes longer to reach the observer than that from point C. So in the light curve, B shifts to B', and so on. Due to this, the light curve gets distorted as shown. The peak position of the time-delay curve is arbitrary because the choice of the reference point for the time delay (point C in this case) is arbitrary. So time delay “bends peaks to the left.” Note that in any case, no shift in peak position is observable, since the observer sees only one light curve, the one including all effects. We discuss the shifts here merely to understand our results the better.

Doppler.—In the above case, the observed flux from a certain point is determined only by the $\cos \psi$ factor in equation (1). When we include the Doppler effect, relativistic beaming comes into the picture. In our simple case, beaming of radiation toward the observer is maximum at point E, while $\cos \psi$ is maximum at point C. So the peak occurs at some intermediate point D. The Doppler effect thus shifts the peak of the light curve. The intensity of the peak also increases dramatically because the spot has a significant velocity along the observer’s line of sight at that point. For other geometries where the spot always moves almost perpendicular to the line of sight, beaming reduces the peak intensity.

General relativity.—Without general relativistic effects, the visible portion of the star is determined by $\cos \psi > 0$. When

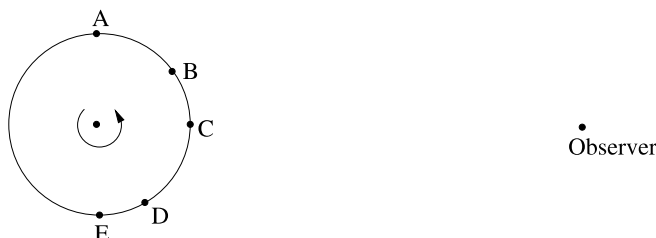


FIG. 4.—Geometry for the case of a single point spot on the equator with the observer in the equatorial plane.

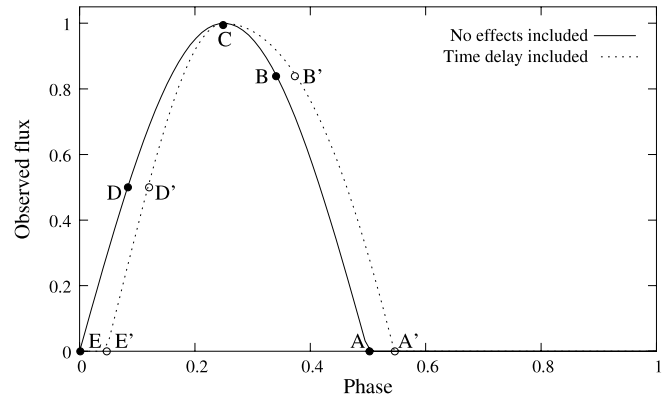


FIG. 5.—Schematic light curve for the case shown in Fig. 4 with and without including time delay, over a period of one rotation of the star. The flux has arbitrary units.

we include general relativistic effects, this condition changes to $\cos \alpha > 0$, with α given by equation (3). Since $\cos \alpha > \cos \psi$, this condition implies that more than half of the stellar surface is visible to the observer at any time. For certain geometries and with antipodal hot spots, this makes both the spots visible simultaneously. In such a case, if the spots are identical, the observed flux is almost constant for the duration for which both spots are visible (see Beloborodov 2002 for a detailed discussion). Even when only one spot is visible, the reduced modulation of the flux (due to $\cos \alpha > \cos \psi$) flattens the light curve. The peak position does not change, however, since the peak occurs when $\cos \alpha$ is maximum, which is when $\cos \psi$ is maximum. Gravitational redshift decreases the total observed flux, except when both the antipodal spots are simultaneously visible, in which case the observed flux can increase.

4.2. Gaussian Spots

To illustrate the above effects, we show some variability curves for spots with a Gaussian flux distribution, maximum at the center and tapering outward. We consider a hypothetical

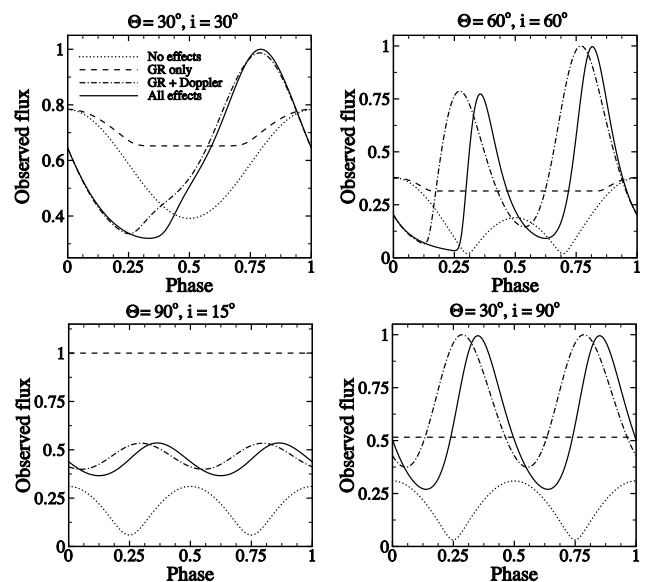


FIG. 6.—Examples of relativistic and light-travel time effects on the light curves for Gaussian spots. Dotted curves do not include any effects, dashed curves include only general relativistic effects, dash-dotted curves include general relativistic and Doppler effects, and solid curves include all effects. The fluxes are normalized.

neutron star with $R = 10$ km and $M = 1.4 M_{\odot}$. To bring out clearly the effects of rotation, we choose a very small rotation period $P = 0.5$ ms. The spots have a width of 10° . Figure 6 shows some variability curves for different misalignment angles Θ and observer inclination angles i . (The inclination angle is the angle between the observer's direction and the star's rotation axis.) We show the curves over one rotation period of the star, since, because of the assumptions in our variability model, the curves are perfectly periodic with a period equal to the star's spin period. Without including any effects, the light curve has one or two peaks depending on whether one or both the hot spots are seen during one rotation period (see R04 for a detailed discussion). General relativistic effects reduce the pulse fraction and, in the cases where both hot spots are simultaneously visible for some time, completely flatten the light curve for that duration. The time-delay effect is seen to distort the light curves. We also see that the Doppler and time-delay effects increase the pulse fraction. These two effects are strongest when the hot spots are moving almost directly toward or away from the observer, which happens at large inclination angles.

5. VARIABILITY CURVES FOR REALISTIC SPOTS

We now turn our attention to the realistic spots discussed in § 2. To calculate the variability curves, we make the following assumptions: only radiation from the hot spots contributes to the light curve; when the infalling matter falls on the star, its entire kinetic and thermal energy is converted into radiation, which is emitted isotropically; the emitted radiation does not interact with the accreting matter. In addition, recall that the hot spots keep changing, but only slightly, with time. So to model the light curves, we choose the hot spots at a certain time and then assume those hot spots to be unchanging. Figure 7 shows the variability curves for the realistic spots in the PW case. The neutron star has $P = 3$ ms. We see that general relativistic effects are the strongest. Even at such a large rotation speed, the effects of rotation are relatively small, which justifies neglecting frame-dragging effects.

For clarity, Figure 8 shows the final light curves (*solid lines*) after including all effects, for different misalignment and inclina-

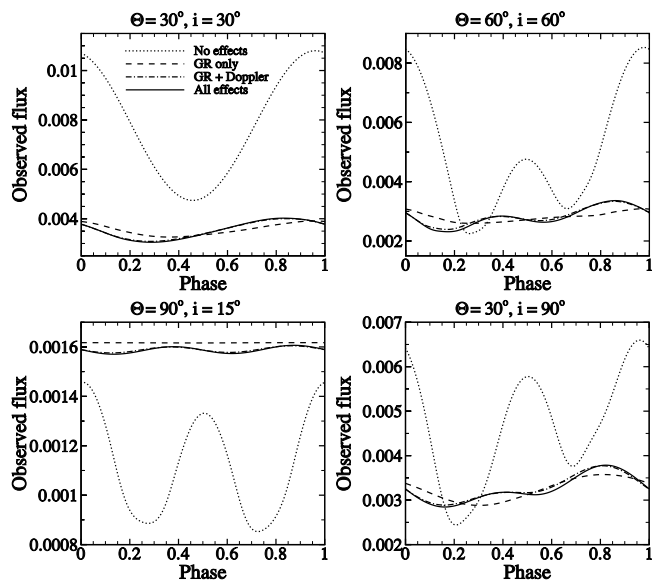


FIG. 7.—Examples of relativistic and light-travel time effects on the light curves of 3 ms pulsars for realistic spots in the PW case. The line patterns mean the same as in Fig. 6.

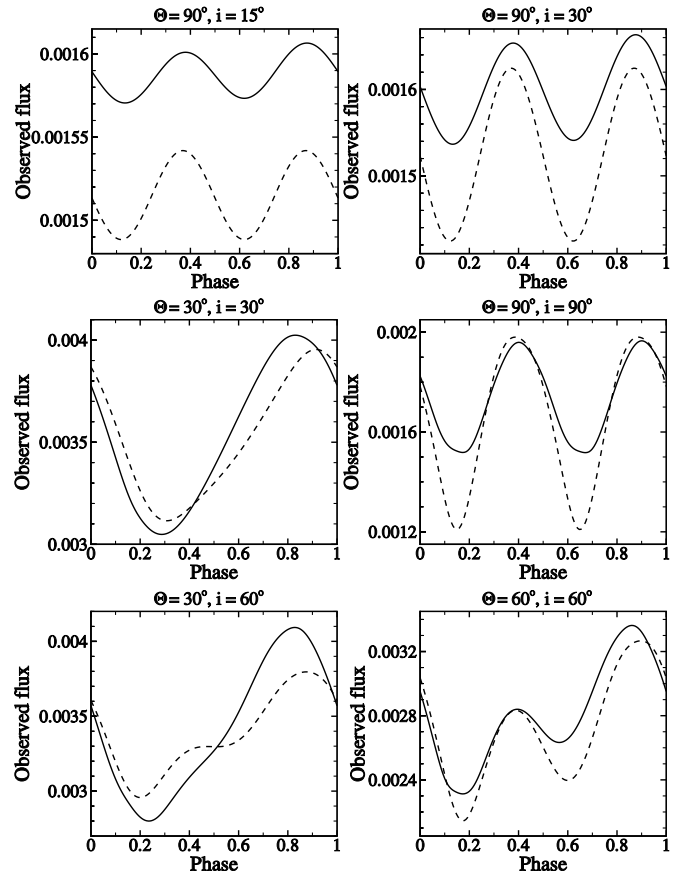


FIG. 8.—Final light curves, including all effects (*solid lines*), with best-fit Gaussian-spot light curves (*dashed lines*), for realistic spots in the PW case for 3 ms pulsars. The pulse fractions are 2% and 8%, respectively, for the top two panels, $\sim 25\%$ – 30% for the middle two, and $\sim 35\%$ – 40% for the bottom two.

tion angles. The curves are almost sinusoidal for small inclination angles when Doppler and time-delay distortions are relatively weaker, and deviate noticeably from a sinusoidal shape for larger inclination angles. The pulse fractions depend on the misalignment and inclination angles and the shape of the hot spots. In most cases the pulse fractions are seen to be quite large compared to the observed values of a few percent for real stars. We see small pulse fractions in our simulations when the misalignment angle or the inclination angle is of the order of a few degrees. The most probable reason, then, for the small pulse fractions of real pulsars is that they have misalignment angles of the order of a few degrees. Another possible explanation is that scattering of the hot spot radiation by the surrounding matter reduces the amplitude of oscillations (Brainerd & Lamb 1987).

We compared the light curves from realistic spots with those from Gaussian ones (Fig. 8, *dashed lines*). We noted that the hot spots for the $\Theta = 30^{\circ}$ case are the most amenable to approximation by Gaussian spots. Thus, we approximated them with Gaussian spots of the same width (34° in this case). The hot spots for the $\Theta = 60^{\circ}$ and 90° cases depart significantly from a round shape, but we tried approximating them with Gaussian spots of the same width as for the $\Theta = 30^{\circ}$ case. The Gaussian spots are centered at the magnetic poles in each case. Their intensity in each case was chosen such that the total flux from the star as seen by a distant observer looking at the spot from directly above the magnetic pole would be the same as that in the case of the realistic spots. We also set the two antipodal hot spots to be identical. The light curves thus obtained are also shown in Figure 8.

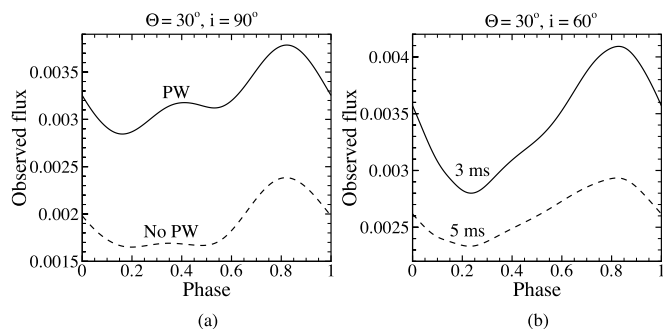


FIG. 9.—(a) Comparison of PW (solid line) and non-PW (dashed line) light curves, including all effects. (b) Comparison of light curves for 3 ms (solid line) and 5 ms (dashed line) pulsars, including all effects.

The fractional rms errors are $<5\%$ for small ($\lesssim 60^\circ$) inclination angles and are $\sim 5\%–10\%$ for large ($\gtrsim 60^\circ$) inclination angles. The two main reasons for Gaussian spots not reproducing the light curves perfectly are that the shapes of the realistic hot spots are more complicated than Gaussian and that the two antipodal hot spots are not usually identical. Figure 9a compares the variability curves for two identical geometries in the PW and non-PW cases. The hot spots, and hence the variability curves, have similar shapes in the two cases. We found that the flux in the PW case is a few times higher than that in the non-PW case in general, as expected from the hot spots shown in Figure 2. However, the pulse fractions turned out to be smaller in the PW case.

We also compared the variability curves of 3 and 5 ms neutron stars for two identical geometries. The results are shown in Figure 9b. The shapes of the hot spots and curves are again similar in these two cases. Both the average flux and pulse fraction are higher for the 3 ms star.

We plotted the observed stellar image for our fiducial 3 ms pulsar in the PW case with and without general relativistic effects, for $\Theta = 90^\circ$ and $i = 15^\circ$, shown in Figure 10. We see that both the antipodal hot spots are visible simultaneously in this case. Figure 3b shows that due to bending of light, the star should

look larger than it actually is, which is also seen here. We do not take the Doppler and time-delay effects into account in these images, since those effects are not noticeable in the images.

6. CONCLUSIONS

We modeled the light curves of accreting millisecond pulsars using hot spots obtained in full three-dimensional MHD simulations done using the Paczyński-Wiita potential, for 3 and 5 ms period pulsars. We found that the main effect of the Paczyński-Wiita potential is to *increase the accretion rate and the emitted flux*. The variability curves in our model are strongly affected by general relativistic effects and to a lesser extent by Doppler, time-delay, and frame-dragging effects. General relativistic effects decrease the pulse fraction, while Doppler and light-travel time effects increase it and distort the light curve. The amount by which the pulse fraction changes, and the distortion of the light curve, depend on the hot spots' position and shape, which are determined by the misalignment angle, and on the observer inclination angle. The small pulse fractions observed in real pulsars suggest that they might have small misalignment angles, of the order of a few degrees.

We compared the light curves from the realistic hot spots that we obtained from our MHD simulations with those from simple hot spots with a Gaussian flux distribution centered at the magnetic poles. We found that the Gaussian-spot light curves differ from the realistic-spot light curves by $<10\%$ and that therefore Gaussian spots are a reasonable approximation for the realistic ones. We plan to investigate in the future how the size and intensity of these equivalent Gaussian spots depend on physical parameters pertaining to the star and the disk.

Numerical variability models, along with analytical models, are important tools for studying periodic and quasi-periodic oscillations from X-ray pulsars. In the region near the star, hot spots, funnel streams, and features in the accretion disk such as density waves could be responsible for producing these oscillations. Our three-dimensional simulations are useful for studying these features. However, a more accurate model of the variability curves, which takes into account emission and absorption of radiation by the accreting matter, and temporal changes in the

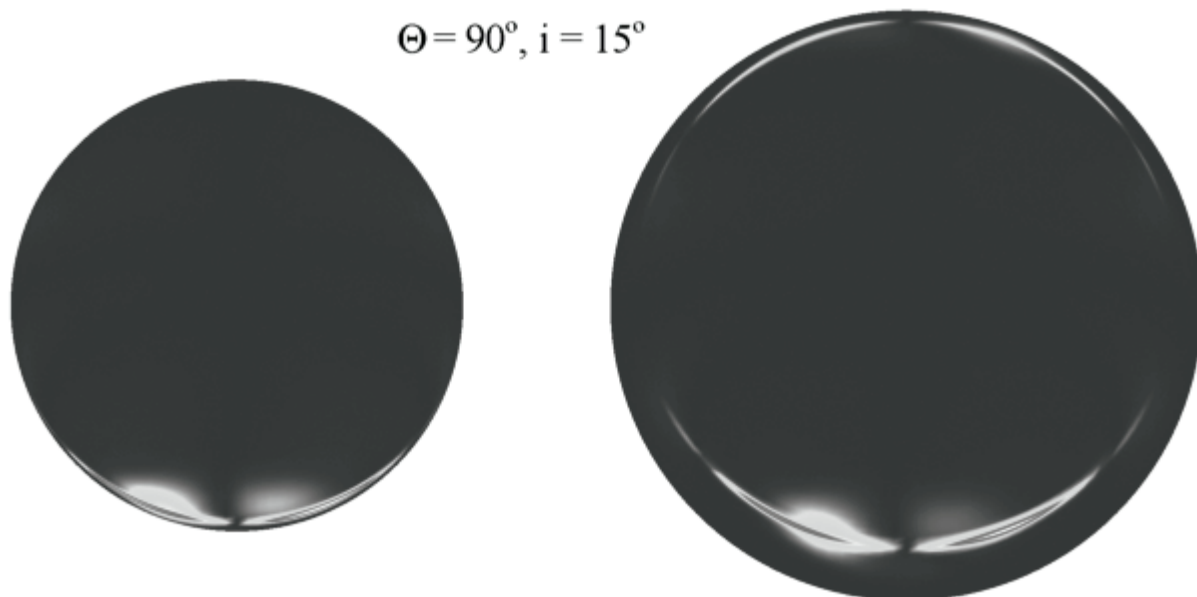


FIG. 10.—Observed stellar image, without including any effects (left) and including general relativistic effects (right). Note the apparent enlargement of the stellar image and the simultaneous visibility of both antipodal hot spots because of general relativistic effects.

hot spots, is needed to determine the role of these features in producing the oscillations. In addition, one of the major simplifications in our model is that we ignore the dynamics of the matter after it falls on the star's surface. This is not a good assumption for millisecond pulsars, where thermonuclear burning of the matter falling on the stellar surface is a possibility (Joss & Li 1980; Bildsten & Brown 1997; Bhattacharyya et al. 2005), which could change the dynamics of the matter flow and magnetic field around the star, especially since the magnetic field is relatively weak. In that case, the hot spots would serve to give

an idea of the place where matter would accumulate and thermonuclear burning could start.

This work was supported in part by NASA grants NAG5-13220 and NAG5-13060 and by NSF grant AST 03-07817. The authors thank A. V. Koldoba and G. V. Ustyugova for developing the code used in our simulations, the referee for valuable comments that greatly improved the paper, and J. Poutanen for valuable suggestions.

REFERENCES

- Beloborodov, A. M. 2002, *ApJ*, 566, L85
 Bhattacharyya, S., Strohmayer, T. E., Miller, M. C., & Markwardt, C. B. 2005, *ApJ*, 619, 483
 Bildsten, L., & Brown, E. 1997, *ApJ*, 477, 897
 Brainerd, J., & Lamb, F. K. 1987, *ApJ*, 317, L33
 Braje, T. M., Romani, R. W., & Rauch, K. P. 2000, *ApJ*, 531, 447
 Chakrabarty, D., Morgan, E. H., Muno, M. P., Galloway, D. K., Wijnands, R., van der Klis, M., & Markwardt, C. B. 2003, *Nature*, 424, 42
 Ford, E. C. 2000, *ApJ*, 535, L119
 Ftaclas, C., Kearney, M. W., & Pechenick, K. 1986, *ApJ*, 300, 203
 Ghosh, P., & Lamb, F. K. 1978, *ApJ*, 223, L3
 ———. 1979, *ApJ*, 232, 259
 Hawley, J. F., & Krolik, J. H. 2001, *ApJ*, 548, 348
 Joss, P. C., & Li, F. K. 1980, *ApJ*, 238, 287
 Koldoba, A. V., Romanova, M. M., Ustyugova, G. V., & Lovelace, R. V. E. 2002, *ApJ*, 576, L53
 Lamb, F. K., Pethick, C. J., & Pines, D. 1973, *ApJ*, 184, 271
 Misner, C. W., Thorne, K. S., & Wheeler, J. A. 1973, *Gravitation* (San Francisco: Freeman)
 Novikov, I., & Thorne, K. S. 1973, in *Black Holes*, ed. B. DeWitt & C. DeWitt (New York: Gordon & Breach), 409
 Paczyński, B., & Wiita, P. J. 1980, *A&A*, 88, 23
 Pechenick, K. R., Ftaclas, C., & Cohen, J. M. 1983, *ApJ*, 274, 846
 Poutanen, J., & Gierlinski, M. 2003, *MNRAS*, 343, 1301
 Pringle, J. E., & Rees, M. J. 1972, *A&A*, 21, 1
 Romanova, M. M., Ustyugova, G. V., Koldoba, A. V., & Lovelace, R. V. E. 2002, *ApJ*, 578, 420
 ———. 2004, *ApJ*, 610, 920 (R04)
 Romanova, M. M., Ustyugova, G. V., Koldoba, A. V., Wick, J. V., & Lovelace, R. V. E. 2003, *ApJ*, 595, 1009
 Shakura, N. I., & Sunyaev, R. A. 1973, *A&A*, 24, 337
 Stella, L., & Vietri, M. 1999, *Phys. Rev. Lett.*, 82, 17
 Terrell, J. 1959, *Phys. Rev.*, 116, 1041
 van der Klis, M. 2000, *ARA&A*, 38, 717
 Viironen, K., & Poutanen, J. 2004, *A&A*, 426, 985
 Wijnands, R. 2005, in *Trends in Pulsar Research*, ed. J. A. Lowry (New York: Nova Science), in press (astro-ph/0501264)
 Wijnands, R., van der Klis, M., Homan, J., Chakrabarty, D., Markwardt, C. B., & Morgan, E. H. 2003, *Nature*, 424, 44